Defence Technology xxx (xxxx) xxx

Contents lists available at ScienceDirect

Defence Technology

journal homepage: www.keaipublishing.com/en/journals/defence-technology

Static and free vibration analyses of functionally graded porous variable-thickness plates using an edge-based smoothed finite element method

Trung Thanh Tran [a], Quoc-Hoa Pham [b, c, *], Trung Nguyen-Thoi [b, c]

[a] Department of Mechanics, Le Quy Don Technical University, Hanoi, Viet Nam
[b] Division of Computational Mathematics and Engineering, Institute for Computational Science, Ton Duc Thang University, Ho Chi Minh City, Viet Nam
[c] Faculty of Civil Engineering, Ton Duc Thang University, Ho Chi Minh City, Viet Nam

ARTICLE INFO

Article history:
Received 12 April 2020
Received in revised form
19 May 2020
Accepted 1 June 2020
Available online xxx

Keywords:
Functionally graded porous (FGP) plates
Edge-based smoothed finite element method (ES-FEM)
Mixed interpolation of tensorial components (MITC)
Static bending
Free vibration

ABSTRACT

The main purpose of this paper is to present numerical results of static bending and free vibration of functionally graded porous (FGP) variable-thickness plates by using an edge-based smoothed finite element method (ES-FEM) associate with the mixed interpolation of tensorial components technique for the three-node triangular element (MITC3), so-called ES-MITC3. This ES-MITC3 element is performed to eliminate the shear locking problem and to enhance the accuracy of the existing MITC3 element. In the ES-MITC3 element, the stiffness matrices are obtained by using the strain smoothing technique over the smoothing domains formed by two adjacent MITC3 triangular elements sharing an edge. Materials of the plate are FGP with a power-law index (k) and maximum porosity distributions (Ω) in the forms of cosine functions. The influences of some geometric parameters, material properties on static bending, and natural frequency of the FGP variable-thickness plates are examined in detail.

1. Introduction

In recent years, FGP material has attracted great interest from researchers over the world due to porosity appeared in materials during the manufacturing process or intentionally created. Porosities inside materials can be distributed with many different types. They can be distributed uniform, non-uniform, or graded function. Basically, porosity reduces the stiffness of the structure, however with engineering properties such as lightweight, excellent energy-absorbing capability, great thermal resistant properties and so on, they still have been widely applied in various fields including aerospace, automotive industry, and civil engineering. A lot of analytical and numerical studies on the FGP structures have been performed and some of typical work can be summarized as follows. Kim et al. [1] investigated the static bending, free vibration, and buckling of FGP micro-plates using modified couples stress base on the analytical method (AM). Barati and Zenkour [2] analyzed the vibration of the FGP cylindrical shells reinforced by the graphene platelet (GPL) using first-order shear deformation theory (FSDT) and Galerkin's method. Zenkour [3] developed a new Quasi-3D to calculate the bending of the FGP plates. Zenkour and Barati [4] considered electro-thermoelastic vibration of FGP plates integrated with piezoelectric layers by using AM and they also investigated post-buckling of FG beams reinforced by GPL with geometrical imperfection [5]. Daikh and Zenkour analyzed the influence of porosity on the bending of FG sandwich plates [6] and calculated free vibration and buckling of FG sandwich plates in Ref. [7]. Sobhy et al. [8] considered the effect of porosity distribution to buckling and free vibration of FG nanoplate using quasi-3D refined theory. Mashat and his co-workers [9] used a quasi 3-D higher-order deformation theory (HSDT) to analyze the bending of FGP plates resting on elastic foundations (EF) under hygro-thermo-mechanical loads. Nguyen et al. developed the polygonal finite element method (PFEM) combined with HSDT to calculate nonlinear static and dynamic responses of FGP plates [10], static bending and free vibration of FGP plates reinforced by GPL [11], and active-controlled

* Corresponding author. Division of Computational Mathematics and Engineering, Institute for Computational Science, Ton Duc Thang University, Ho Chi Minh City, Viet Nam.
E-mail address: phamquochoa@tdtu.edu.vn (Q.-H. Pham).
Peer review under responsibility of China Ordnance Society

https://doi.org/10.1016/j.dt.2020.06.001

vibration of FGP plate reinforced by GPL [12]. In addition, Nguyen et al. [13] controlled of geometrically nonlinear responses of smart FGP plates reinforced GPL based on Bézier extraction of the Non-Uniform Rational B-Spline (NURBS). Rezaei [14,15] based on AM to examine the free vibration of rectangular and porous-cellular plates. Zhao et al. [16] investigated the free vibration of FGP shallow shells using an improved Fourier method, and then analyzed the dynamics of the FGP doubly-curved panels and shells [17]. Li et al. [18] analyzed nonlinear vibration and dynamic buckling of the sandwich FGP plate reinforced GPL on the elastic foundation (EF). With the nonlinear problem, Sahmani et al. [19] used the nonlocal method to analyze nonlinear large-amplitude vibrations of FGP micro/nano-plates with GPL reinforce. Wu et al. [20] considered the dynamic of FGP structures by using FEM.

Variable-thickness structures are extensively used in many types of high-performance surfaces like aircraft, civil engineering, and other engineering fields. Using these structures will help adjust the weight of structural, and hence help maximize the capacity of the material. Gagnon and Gosselin [21] studied the static bending of variable thickness homogeneous plates using the finite strip method (FSM). Sakiyama et al. [22] analyzed the free vibration homogeneous plates using the function approximation method (FAM). Singh and Saxena [23] considered a rectangular variable-thickness plate using the Rayleigh-Ritz method based on basis functions satisfying essential boundary conditions (BC). Nerantzaki and Katsikades [24] used an analog equation solution to analyze the free vibration and dynamic behaviors of the variable-thickness plates. Mikami and Yoshimura [25] have applied the collocation method with orthogonal polynomials to calculate the natural frequencies for linear variable-thickness plates based on Reissner–Mindlin plate theory. Al-Kaabi and his colleagues have shown a method based on a variational principle in conjunction with finite difference technique for analysis of the Reissner-Mindlin plate of linearly [26] and parabolically [27] varying thickness. Based on the FSDT, Mizusawa et al. [28] have developed the spline strip method to study the natural frequencies for the tapered rectangular plates. All of these papers only investigate plates with two opposite simply supported (SS) edges perpendicular to the direction of thickness variation. Cheung et al. [29] calculated the free vibration of Reissner-Mindlin variable-thickness plates using the Rayleigh-Ritz method with different BC. Manh and Nguyen [30] combined FSDT with isogeometric analysis (IGA) to study the static bending and buckling of the composite variable-thickness plates. Lieu et al. [31] based on the IGA to compute static bending and free vibration of bi-directional FGM variable-thickness plates. Gupta et al. [32] examined the influence of crack location on the vibration of non-uniform thickness FGM micro-plate and in Ref. [33] Dhurvey simulated the buckling of the composite variable-thickness plates using ANSYS software. Thang et al. [34] investigated the effects of variable thickness on buckling and post-buckling of imperfect sigmoid FGM plates on elastic medium (EM) subjected to compressive loading. Thien et al. [35] developed the IGA to analyze buckling analysis of non-uniform thickness nanoplates in an EM. In addition, Zenkour [36] presented hygrothermal mechanical bending of variable-thickness plates using AM. In Ref. [37], Allam and his colleagues investigated thermoelastic stresses in FG variable-thickness rotating annular disks using infinitesimal theory.

To improve the convergence and accuracy of the plate and shell structural analyses, the origin MITC3 element [38] is combined with the ES-FEM [39] to give the so-called ES-MITC3 element [40–45]. In the formulation of the ES-MITC3, the system stiffness matrix is employed using strains smoothed over the smoothing domains associated with the edges of the triangular elements. The numerical results of the present study demonstrated that the ES-MITC3 has the following superior properties [40]: (1) the ES-MITC3 can avoid transverse shear locking phenomenon even with the ratio of the thickness to the length of the structures reach 10^{-8}; (2) the ES-MITC3 has higher accuracy than the existing triangular elements such as MITC3 [38], DSG3 [46] and CS-DSG3 [47]; and is a good competitor with the quadrilateral element MITC4 element [48].

According to the best of authors' knowledge, static bending and free vibration analyses of FGP variable-thickness plates using ES-MITC3 have not yet been published, especially with the variable thickness of FGP plates in both directions with any BC. Therefore, this paper aims to fill in this gap by developing the ES-MITC3 method for static bending and free vibration analyses of the FGP variable-thickness plates. The formulation is based on the FSDT due to its simplicity and computational efficiency. The accuracy and reliability of the present approach are verified by comparing with those of other available numerical results. Moreover, the numerical and graphical results illustrate the effect of maximum porosity value, power-law index, and the law of variable thickness on the static bending and free vibration of FGP plates.

2. The FGP variable-thickness plates

Consider an FGP variable-thickness plate as depicted in Fig. 1 which has laws of variable thickness are shown in Fig. 2. Type 1: the plate has a constant thickness as shown in Fig. 2(a); Type 2: the thickness varies linearly in the x-axis as shown in Fig. 2(b); Type 3: the thickness varies linearly in the x-axis and y-axis as shown in Fig. 2(c).

The FGP with the variation of two constituents and three different distributions of porosity through thickness are presented as [1]:

$$\begin{aligned}
&\text{Case 1}: \quad \Phi(z) = \Omega\cos\left(\frac{\pi z}{h}\right)\\
&\text{Case 2}: \quad \Phi(z) = \Omega\cos\left[\frac{\pi}{2}\left(\frac{z}{h}+0.5\right)\right]\\
&\text{Case 3}: \quad \Phi(z) = \Omega\cos\left[\frac{\pi}{2}\left(\frac{z}{h}-0.5\right)\right]
\end{aligned} \tag{1}$$

in which Ω is the maximum porosity value. The typical material properties of FGP in the thickness direction of the plate are given by the rule:

$$P(z) = \left[(P_t - P_b)\left(\frac{z}{h}+0.5\right)^k + P_b\right](1-\Phi(z)) \tag{2}$$

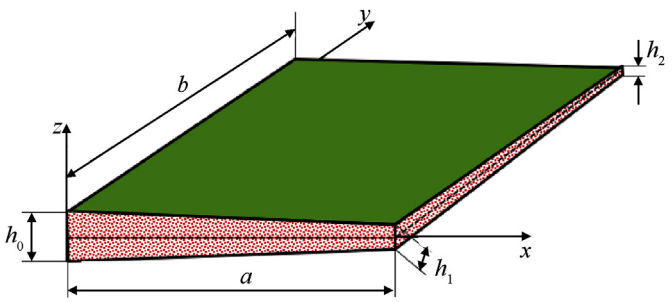

Fig. 1. The FGP plate model with varying thickness.

Please cite this article as: Tran TT et al., Static and free vibration analyses of functionally graded porous variable-thickness plates using an edge-based smoothed finite element method, Defence Technology, https://doi.org/10.1016/j.dt.2020.06.001

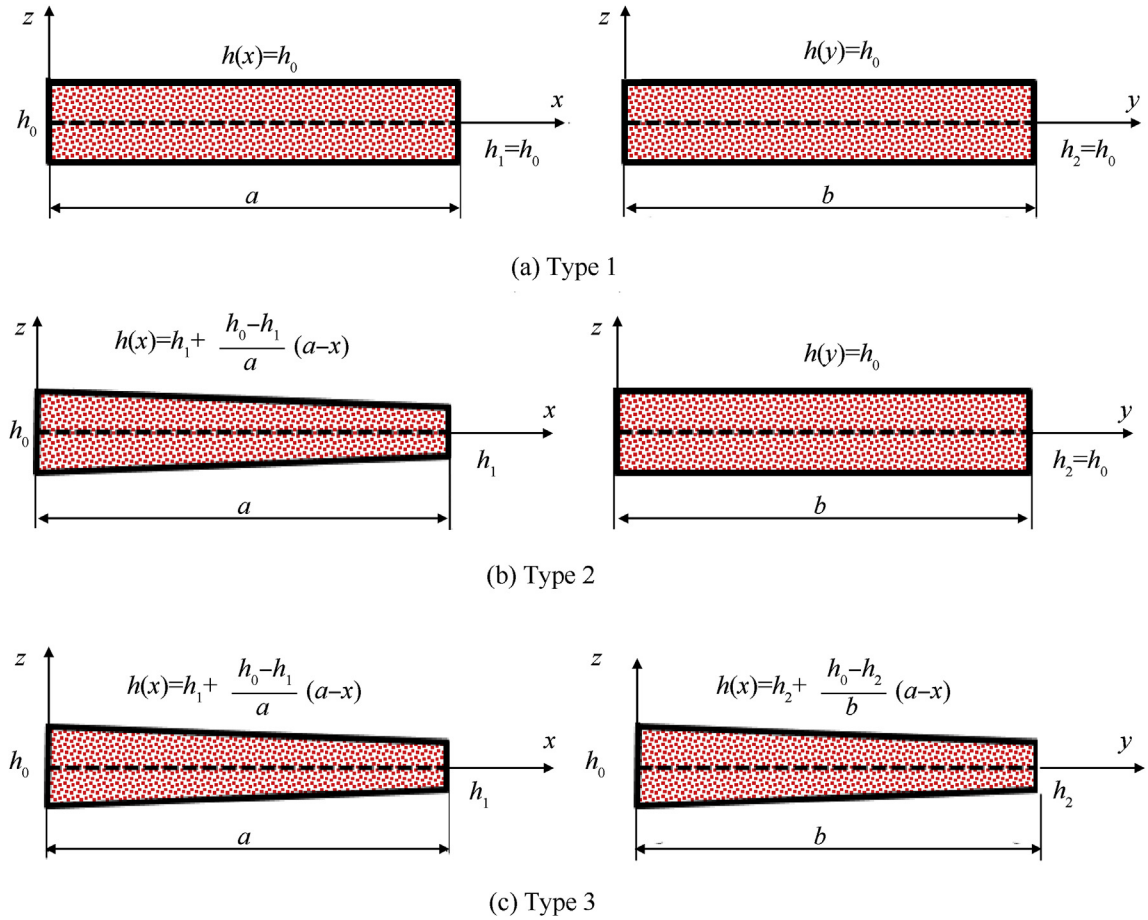

Fig. 2. The laws of variable thickness of FGP plates.

where P_t and P_b are the typical material properties at the top and the bottom surfaces, respectively and k is the power-law index. Fig. 3(a) shows the normalized distribution of porosity through-thickness. Fig. 3(b), (c), (d) show the normalized distributions of three different cases of porosity in which $\mathbf{\Omega} = 0.5$, $k = 0.5, 1, 10$, and P_t/P_b=10. The porosity distribution of Case 1 is symmetric with respect to the mid-plane of plates and a center enhanced distribution. Case 2 and Case 3 are bottom and top surface-enhanced distributions, respectively. From Fig. 3(a–c), we can see that all cases of distribution porosity increase the hardness of the upper surface of the plate, however, case 3 increases the stiffness of the plate through thickness as not strongly as the other two cases.

3. The weak form and FEM formulation for FGP plates

3.1. The first order shear deformation theory for FGP plates

The displacement fields of FGP plate in present work based on FSDT model can be expressed as [49]:

$$\begin{cases} u(x,y,z) = u_0(x,y) + z\theta_x(x,y) \\ v(x,y,z) = v_0(x,y) + z\theta_y(x,y)) \\ w\,(x,y,z) = w_0(x,y) \end{cases} \tag{3}$$

in which u_0, v_0, w_0 denotes displacement variables of mid-surface of the plate $(z = 0)$ and θ_x, θ_y are the rotations of a transverse normal about the y-axis and x-axis, respectively.

For the bending plate, the strain components can be expressed as follows:

$$\boldsymbol{\varepsilon} = \boldsymbol{\varepsilon}_m + z\boldsymbol{\kappa} \tag{4}$$

with the membrane strain

$$\boldsymbol{\varepsilon}_m = \begin{Bmatrix} u_{0,x} \\ v_{0,y} \\ u_{0,y} + v_{0,x} \end{Bmatrix} \tag{5}$$

and the bending strain

$$\boldsymbol{\kappa} = \begin{Bmatrix} \theta_{x,x} \\ \theta_{y,y} \\ \theta_{x,y} + \theta_{y,x} \end{Bmatrix} \tag{6}$$

and the transverse shear strain is expressed by:

$$\boldsymbol{\gamma} = \begin{Bmatrix} w_{0,x} + \theta_x \\ w_{0,y} + \theta_y \end{Bmatrix} \tag{7}$$

From Hooke's law, the linear stress-strain relations of the FGP plates can be expressed as:

Please cite this article as: Tran TT et al., Static and free vibration analyses of functionally graded porous variable-thickness plates using an edge-based smoothed finite element method, Defence Technology, https://doi.org/10.1016/j.dt.2020.06.001

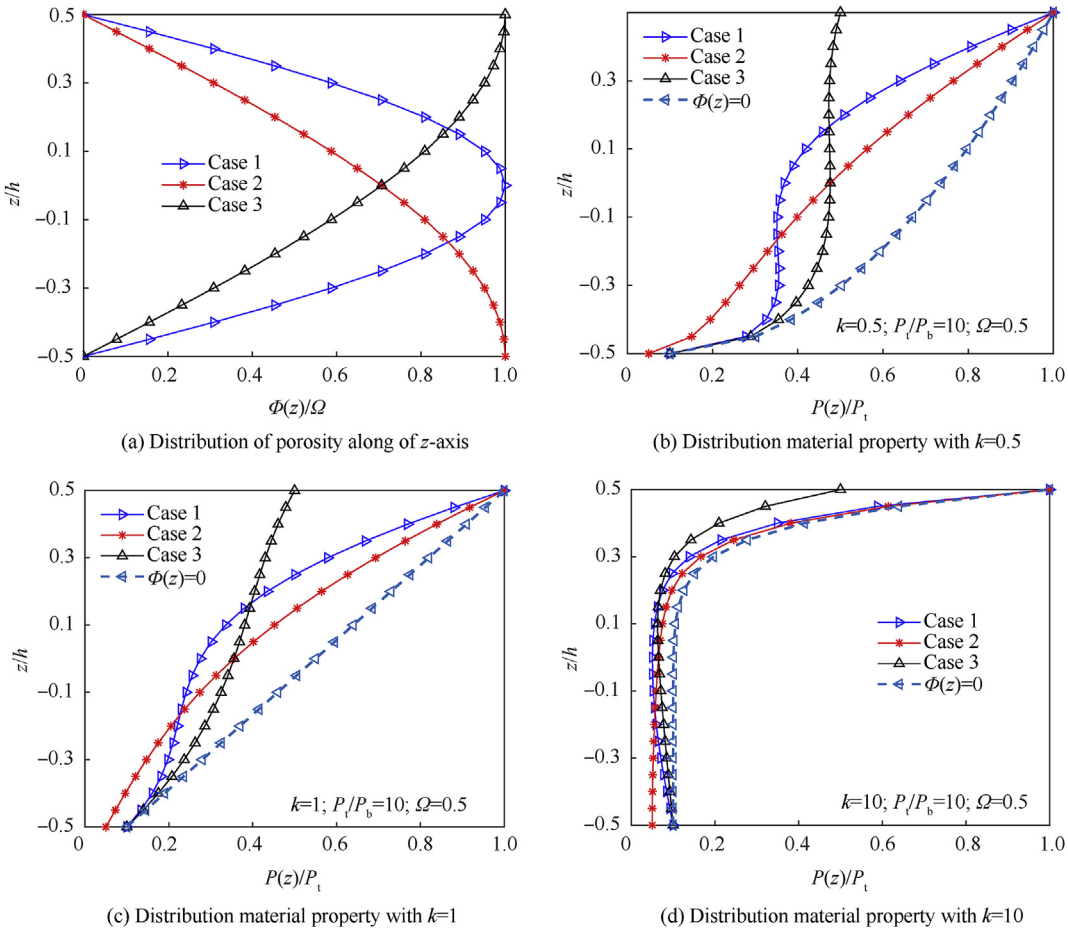

(a) Distribution of porosity along of z-axis

(b) Distribution material property with k=0.5

(c) Distribution material property with k=1

(d) Distribution material property with k=10

Fig. 3. Distribution of porosity and typical material property.

$$\begin{Bmatrix} \sigma_x \\ \sigma_y \\ \tau_{xy} \\ \tau_{xz} \\ \tau_{yz} \end{Bmatrix} = \begin{bmatrix} Q_{11} & Q_{12} & 0 & 0 & 0 \\ Q_{21} & Q_{22} & 0 & 0 & 0 \\ 0 & 0 & Q_{66} & 0 & 0 \\ 0 & 0 & 0 & Q_{55} & 0 \\ 0 & 0 & 0 & 0 & Q_{44} \end{bmatrix} \begin{Bmatrix} \varepsilon_x \\ \varepsilon_y \\ \gamma_{xy} \\ \gamma_{xz} \\ \gamma_{yz} \end{Bmatrix} \tag{8}$$

where

$$Q_{11} = Q_{22} = \frac{E(z)}{1-\upsilon(z)^2}; \quad Q_{12} = Q_{21} = \frac{\upsilon(z)E(z)}{1-\upsilon(z)^2}; \quad Q_{44} = Q_{55} = Q_{66} = \frac{E(z)}{2(1+\upsilon(z))} \tag{9}$$

in which $E(z)$, $\upsilon(z)$ are the effective Young's modulus, Poisson's ratio which is calculated by Eq. (2), respectively.

3.2. Weak form equations

To obtain the governing equations of the FGP plates, the Hamilton's principle is applied in the following form [49]:

$$\int_{t_1}^{t_2} (\delta \mathscr{U} + \delta \mathscr{V} - \delta \mathscr{K}) \mathrm{d}t = 0 \tag{10}$$

where $\mathscr{U}$, $\mathscr{V}$ and $\mathscr{K}$ are the strain energy, the work done by external loads and the kinetic energy of plate, respectively.

The strain energy is expressed as:

$$\mathscr{U} = \frac{1}{2}\int_{\Psi} \left(\boldsymbol{\varepsilon}^{\mathrm{T}} \boldsymbol{D}_b \boldsymbol{\varepsilon} + \boldsymbol{\gamma}^{\mathrm{T}} \boldsymbol{D}_s \boldsymbol{\gamma} \right) \mathrm{d}\Psi \tag{11}$$

in which $\boldsymbol{\varepsilon} = [\boldsymbol{\varepsilon}_m \boldsymbol{\kappa}]^{\mathrm{T}}$ and

$$\boldsymbol{D}_b = \begin{bmatrix} \boldsymbol{A} & \boldsymbol{B} \\ \boldsymbol{B} & \boldsymbol{D} \end{bmatrix} \tag{12}$$

with $\boldsymbol{A}$, $\boldsymbol{B}$, $\boldsymbol{D}$, and $\boldsymbol{D}_s$ can be given by

$$(\boldsymbol{A}, \boldsymbol{B}, \boldsymbol{D}) = \int_{-h(x,y)/2}^{h(x,y)/2} \left(1, z, z^2\right) \begin{bmatrix} Q_{11} & Q_{12} & 0 \\ Q_{21} & Q_{22} & 0 \\ 0 & 0 & Q_{66} \end{bmatrix} \mathrm{d}z \tag{13}$$

Please cite this article as: Tran TT et al., Static and free vibration analyses of functionally graded porous variable-thickness plates using an edge-based smoothed finite element method, Defence Technology, https://doi.org/10.1016/j.dt.2020.06.001

$$\boldsymbol{D}_s = \int_{-h(x,y)/2}^{h(x,y)/2} \begin{bmatrix} Q_{55} & 0 \\ 0 & Q_{44} \end{bmatrix} \mathrm{d}z \tag{14}$$

The work done by external transverse loads are expressed by

$$\mathscr{V} = \int_{\Psi} q\boldsymbol{w}\mathrm{d}\Psi \tag{15}$$

The kinetic energy is given by

$$\mathscr{K} = \frac{1}{2}\int_{\Psi} \dot{\boldsymbol{u}}^{\mathrm{T}}\mathbf{m}\dot{\boldsymbol{u}}\mathrm{d}\Psi \tag{16}$$

in which $\boldsymbol{u}^{\mathrm{T}} = [u_0 v_0 w_0 \theta_x \theta_y]$, and $\boldsymbol{m}$ is the mass matrix defined by:

$$\boldsymbol{m} = \begin{bmatrix} I_1 & 0 & 0 & I_2 & 0 \\ & I_1 & 0 & 0 & I_2 \\ & & I_1 & 0 & 0 \\ & & & I_3 & 0 \\ & & & & I_3 \end{bmatrix} \tag{17}$$

with $(I_1, I_2, I_3) = \int_{-h(x,y)/2}^{h(x,y)/2} \rho(z)(1, z, z^2)\mathrm{d}z$.

As this plate structure has variation thickness, all matrices in Eq. (13), Eq. (14) and Eq. (17) depend on the law of varying thickness. The limits of integration depend on the position of the point on the plate.

Substituting Eqs. (11), (15) and (16) into Eq. (10), the weak formulation for static and free vibration of FGP plates, respectively, is finally obtained as

$$\int_{\Psi} \delta\boldsymbol{\varepsilon}^{\mathrm{T}}\boldsymbol{D}_b\boldsymbol{\varepsilon}\mathrm{d}\Psi + \int_{\Psi} \delta\boldsymbol{\gamma}^{\mathrm{T}}\boldsymbol{D}_s\boldsymbol{\gamma}\mathrm{d}\Psi = \int_{\Psi} q\delta\boldsymbol{w}\mathrm{d}\Psi \tag{18}$$

and

$$\int_{\Psi} \delta\boldsymbol{\varepsilon}^{\mathrm{T}}\boldsymbol{D}_b\boldsymbol{\varepsilon}\mathrm{d}\Psi + \int_{\Psi} \delta\boldsymbol{\gamma}^{\mathrm{T}}\boldsymbol{D}_s\boldsymbol{\gamma}\mathrm{d}\Psi = \int_{\Psi} \ddot{\boldsymbol{u}}^{\mathrm{T}}\mathbf{m}\dot{\boldsymbol{u}}\mathrm{d}\Psi \tag{19}$$

4. Formulation of an ES-MITC3 method for FGP plates

4.1. Formulation of finite element based on the MITC3

The bounded domain Ψ is discretized into n^e MITC3 elements with n^n nodes such that $\Psi \approx \sum_{e=1}^{n^e} \Psi_e$ and $\Psi_i \cap \Psi_j = \varnothing, i \neq j$. Then the generalized displacements at any point $\boldsymbol{u}^e = \left[u_j^e, v_j^e, w_j^e, \theta_{xj}^e, \theta_{yj}^e\right]^{\mathrm{T}}$ for elements of the FGP plate can be approximated as:

$$\boldsymbol{u}^e = \sum_{j=1}^{n^{ne}} \begin{bmatrix} N_I(\mathrm{x}) & 0 & 0 & 0 & 0 \\ 0 & N_I(\mathrm{x}) & 0 & 0 & 0 \\ 0 & 0 & N_I(\mathrm{x}) & 0 & 0 \\ 0 & 0 & 0 & N_I(\mathrm{x}) & 0 \\ 0 & 0 & 0 & 0 & N_I(\mathrm{x}) \end{bmatrix} \boldsymbol{d}_j^e = \sum_{j=1}^{n^{ne}} \boldsymbol{N}(\mathrm{x})\boldsymbol{d}_j^e \tag{20}$$

where n^{ne} is the number of nodes of the plate element; $N(\mathrm{x})$ and $\boldsymbol{d}_j^e = \left[u_j^e, v_j^e, w_j^e, \theta_{xj}^e, \theta_{yj}^e\right]^{\mathrm{T}}$ is the shape function and the nodal degrees of freedom (DOF) of $\boldsymbol{u}^e$ associated with the jth node of the element, respectively.

The linear membrane and the bending strains of the MICT3 element can be expressed in matrix forms as follows

$$\boldsymbol{\varepsilon}_m^e = \left[\boldsymbol{B}_{m1}^e \boldsymbol{B}_{m2}^e \boldsymbol{B}_{m3}^e\right]\boldsymbol{d}^e = \boldsymbol{B}_m^e\,\boldsymbol{d}^e \tag{21}$$

$$\boldsymbol{\kappa}^e = \left[\boldsymbol{B}_{b1}^e \boldsymbol{B}_{b2}^e \boldsymbol{B}_{b3}^e\right]\boldsymbol{d}^e = \boldsymbol{B}_b^e\,\boldsymbol{d}^e \tag{22}$$

where

$$\boldsymbol{B}_{m1}^e = \frac{1}{2A_e}\begin{bmatrix} b-c & 0 & 0 & 0 & 0 \\ 0 & d-a & 0 & 0 & 0 \\ d-a & b-c & 0 & 0 & 0 \end{bmatrix}, \tag{23}$$

$$\boldsymbol{B}_{m2}^e = \frac{1}{2A_e}\begin{bmatrix} c & 0 & 0 & 0 & 0 \\ 0 & -d & 0 & 0 & 0 \\ -d & c & 0 & 0 & 0 \end{bmatrix}, \tag{24}$$

$$\boldsymbol{B}_{m3}^e = \frac{1}{2A_e}\begin{bmatrix} -b & 0 & 0 & 0 & 0 \\ 0 & a & 0 & 0 & 0 \\ a & -b & 0 & 0 & 0 \end{bmatrix}, \tag{25}$$

$$\boldsymbol{B}_{b1}^e = \frac{1}{2A_e}\begin{bmatrix} 0 & 0 & 0 & b-c & 0 \\ 0 & 0 & 0 & 0 & d-a \\ 0 & 0 & 0 & d-a & b-c \end{bmatrix}, \tag{26}$$

$$\boldsymbol{B}_{b2}^e = \frac{1}{2A_e}\begin{bmatrix} 0 & 0 & 0 & c & 0 \\ 0 & 0 & 0 & 0 & -d \\ 0 & 0 & 0 & -d & c \end{bmatrix}, \tag{27}$$

$$\boldsymbol{B}_{b3}^e = \frac{1}{2A_e}\begin{bmatrix} 0 & 0 & 0 & -b & 0 \\ 0 & 0 & 0 & 0 & a \\ 0 & 0 & 0 & a & -b \end{bmatrix}, \tag{28}$$

To eliminate the shear locking phenomenon as the thickness of the plate becomes very small, the MITC3 element based on FSDT is proposed by Lee et al. [38]. In their study, the transverse shear strains of the classical triangular element are independent interpolated by computing at the middle of triangular element edges, named typing points. The transverse shear strain field associated to typing points with 5 DOFs per node can be written as:

$$\boldsymbol{\gamma}^e = \boldsymbol{B}_s^e\,\boldsymbol{d}^e \tag{29}$$

in which

Please cite this article as: Tran TT et al., Static and free vibration analyses of functionally graded porous variable-thickness plates using an edge-based smoothed finite element method, Defence Technology, https://doi.org/10.1016/j.dt.2020.06.001

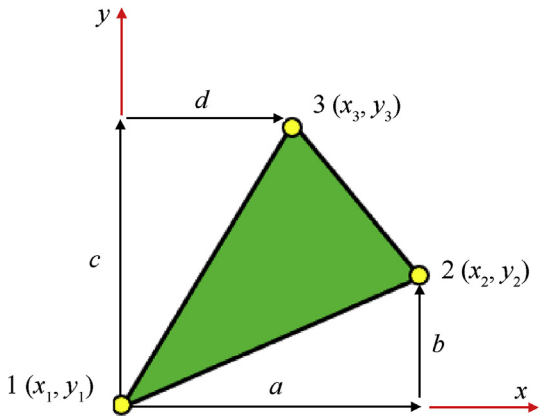

Fig. 4. Three-node triangular element in the local coordinates.

$$\boldsymbol{B}_{\mathrm{s}}^{e} = \left[\boldsymbol{B}_{\mathrm{s}1}^{e}\boldsymbol{B}_{\mathrm{s}2}^{e}\boldsymbol{B}_{\mathrm{s}3}^{e}\right] \tag{30}$$

with

$$\boldsymbol{B}_{\mathrm{s}1}^{e} = \boldsymbol{J}^{-1}\begin{bmatrix} 0 & 0 & -1 & \frac{a}{3}+\frac{d}{6} & \frac{b}{3}+\frac{c}{6} \\ 0 & 0 & -1 & \frac{d}{3}+\frac{a}{6} & \frac{c}{3}+\frac{b}{6} \end{bmatrix} \tag{31}$$

$$\boldsymbol{B}_{\mathrm{s}2}^{e} = \boldsymbol{J}^{-1}\begin{bmatrix} 0 & 0 & 1 & \frac{a}{2}-\frac{d}{6} & \frac{b}{2}-\frac{c}{6} \\ 0 & 0 & 0 & \frac{d}{6} & \frac{c}{6} \end{bmatrix} \tag{32}$$

$$\boldsymbol{B}_{\mathrm{s}3}^{e(0)} = \boldsymbol{J}^{-1}\begin{bmatrix} 0 & 0 & 0 & \frac{a}{6} & \frac{b}{6} & 0 & 0 \\ 0 & 0 & 1 & \frac{d}{2}-\frac{a}{6} & \frac{c}{2}-\frac{b}{6} & 0 & 0 \end{bmatrix} \tag{33}$$

where

$$\boldsymbol{J}^{-1} = \frac{1}{2A_{\mathrm{e}}}[c-b-da] \tag{34}$$

in which $a = x_2 - x_1$, $b = y_2 - y_1$, $c = y_3 - y_1$ and $d = x_3 - x_1$ are pointed out in and A_{e} is the area of the three-node triangular element shown in Fig. 4.

Substituting the discrete displacement field into Eqs. (18) and (19), we obtained the discrete system equations for static and free vibration analysis of the FGP plate using MITC3 based on FSDT formulation, respectively as

$$\boldsymbol{K}\boldsymbol{u} = \boldsymbol{F} \tag{35}$$

where $\boldsymbol{K}$ is the stiffness matrix of FGP plate and $\boldsymbol{F}$ represents the load vector.

$$\boldsymbol{K} = \sum_{e=1}^{n^e}\boldsymbol{K}^e, \quad \boldsymbol{F} = \sum_{e=1}^{n^e}\boldsymbol{F}^e \tag{36}$$

with

$$\boldsymbol{K}^e = \int_{\Psi_{\mathrm{e}}}\boldsymbol{B}^{\mathrm{T}}\boldsymbol{D}_{\mathrm{b}}\boldsymbol{B}\mathrm{d}\Psi_{\mathrm{e}} + \int_{\Psi_{\mathrm{e}}}\boldsymbol{B}_{\mathrm{s}}^{\mathrm{T}}\boldsymbol{D}_{\mathrm{s}}\boldsymbol{B}_{\mathrm{s}}\mathrm{d}\Psi_{\mathrm{e}} \tag{37}$$

where

$$\boldsymbol{B}^{e} = \left[\boldsymbol{B}_{\mathrm{m}}^{e}\ \boldsymbol{B}_{\mathrm{b}}^{e}\right] \tag{38}$$

$$\boldsymbol{F}^{e} = \int_{\Psi_{\mathrm{e}}}\boldsymbol{p}\boldsymbol{N}\mathrm{d}\Psi_{\mathrm{e}} \tag{39}$$

and

$$\left(\boldsymbol{K}-\omega^2\boldsymbol{M}\right)\boldsymbol{u} = 0 \tag{40}$$

where ω is the natural frequency and $\boldsymbol{M}$ is the mass matrix

$$\left(\boldsymbol{K}-\omega^2\boldsymbol{M}\right)\boldsymbol{u} = 0 \tag{41}$$

$$\boldsymbol{M} = \sum_{e=1}^{n^e}\boldsymbol{M}^e \tag{42}$$

$$\boldsymbol{M}^e = \int_{\Omega_e}\boldsymbol{N}^{\mathrm{T}}\boldsymbol{m}\boldsymbol{N}\mathrm{d}\Psi_e \tag{43}$$

4.2. Formulation of an ES-MITC3 method for FGP plates

In the ES-FEM, a domain Ψ is divided into n^k smoothing domains Ψ^k based on edges of elements, such as $\Psi = \cup_{k=1}^{n^k}\Psi^k$ and $\Psi_i^k \cap \Psi_j^k = \varnothing$ for $i \neq j$. An edge-based smoothing domain Ψ^k associated with the inner edge k is formed by connecting two end-nodes of the edge to centroids of adjacent MITC3 elements as shown in Fig. 5.

Now, by applying the ES-FEM [39], the smoothed strain $\tilde{\varepsilon}^k$, a smoothed shear strain $\tilde{\gamma}^k$ over the smoothing domain Ψ^k can be created by computing the integration of the compatible strains, the strain $\boldsymbol{\varepsilon}$ and the shear strain $\boldsymbol{\gamma}$, respectively, in Eqs. (18) and (19) such as:

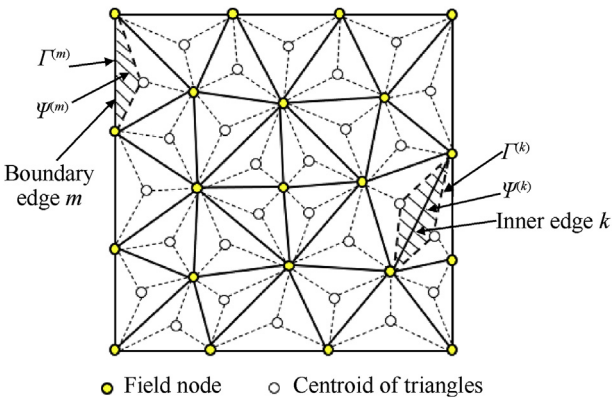

Fig. 5. The smoothing domain Ψ^k is formed by triangular elements.

$$\tilde{\boldsymbol{\varepsilon}}^k = \int_{\Psi^k} \boldsymbol{\varepsilon} \Phi^k(\mathbf{x}) \mathrm{d}\Psi, \tag{44}$$

$$\tilde{\boldsymbol{\gamma}}^k = \int_{\Psi^k} \boldsymbol{\gamma} \Phi^k(\mathbf{x}) \mathrm{d}\Psi, \tag{45}$$

where $\Phi^k(\mathbf{x})$ is a given smoothing function that satisfies at least unity property $\int_{\Psi^k} \Phi^k(\mathbf{x}) \mathrm{d}\Psi = 1$. In this study, we use the constant smoothing function.

$$\Phi^k(\mathbf{x}) = \begin{cases} \dfrac{1}{A^k} x \in \Psi^k \\ 0 \quad x \notin \Psi^k \end{cases} \tag{46}$$

in which A^k is the area of the smoothing domain Ψ^k and is given by

$$A^k = \int_{\Omega^k} \mathrm{d}\Psi = \frac{1}{3} \sum_{i=1}^{n^{ek}} A^i \tag{47}$$

where n^{ek} is the number of the adjacent MITC3 elements in the smoothing domain Ψ^k; and A^i is the area of the ith MITC3 element attached to the edge k.

By substituting Eqs. (21), (22) and (29) into Eqs. (44) and (45) then, the approximation of the smoothed strains on the smoothing domain Ψ^k can be expressed by:

$$\tilde{\boldsymbol{\varepsilon}}_m^k = \sum_{j=1}^{n^{nk}} \tilde{\mathbf{B}}_{mj}^k \boldsymbol{d}_j^k \;\; ; \;\; \tilde{\boldsymbol{\kappa}}^k = \sum_{j=1}^{n_{sh}^{nk}} \tilde{\mathbf{B}}_{bj}^k \boldsymbol{d}_j^k \;\; ; \;\; \tilde{\boldsymbol{\gamma}}^k = \sum_{j=1}^{n_{sh}^{nk}} \tilde{\mathbf{B}}_{sj}^k \boldsymbol{d}_j^k; \tag{48}$$

where n_{sh}^{nk} is the total number of nodes of the MITC3 elements attached to edge k (i.e. $n_{sh}^{nk} = 3$ for boundary edges and $n_{sh}^{nk} = 4$ for inner edges as given in Fig. 5; $\boldsymbol{d}_j^k$ is the nodal DOFs associated with the smoothing domain Ψ^k; $\tilde{\mathbf{B}}_{mj}^k$, $\tilde{\mathbf{B}}_{bj}^k$, and $\tilde{\mathbf{B}}_{sj}^k$ are the smoothed membrane, the smoothed bending, the smoothed shear strain gradient matrices, respectively, at the jth node of the elements attached to edge k and computed by

$$\tilde{\mathbf{B}}_{mj}^k = \frac{1}{A^k} \sum_{i=1}^{n^{ek}} \frac{1}{3} A^i \mathbf{B}_{mj}^e \tag{49}$$

$$\tilde{\mathbf{B}}_{bj}^k = \frac{1}{A^k} \sum_{i=1}^{n^{ek}} \frac{1}{3} A^i \mathbf{B}_{bj}^e \tag{50}$$

$$\tilde{\mathbf{B}}_{sj}^k = \frac{1}{A^k} \sum_{i=1}^{n^{ek}} \frac{1}{3} A^i \mathbf{B}_{sj}^e \tag{51}$$

The global stiffness matrix of FGP plate using the ES-MITC3 is assembled by

$$\tilde{K} = \sum_{k=1}^{n_{sh}^k} \tilde{\boldsymbol{K}}^k \tag{52}$$

where $\tilde{\boldsymbol{K}}^k$ is the ES-MITC3 stiffness matrix of the smoothing domain Ψ^k and given by

$$\tilde{\boldsymbol{K}}^k = \int_{\Psi^k} \left(\tilde{\boldsymbol{B}}^{kT} \boldsymbol{D}_\mathrm{b} \tilde{\boldsymbol{B}}^k + \tilde{\boldsymbol{B}}_\mathrm{s}^{kT} \boldsymbol{D}_\mathrm{s} \tilde{\boldsymbol{B}}_\mathrm{s}^k \right) \mathrm{d}\Psi = \tilde{\boldsymbol{B}}^{kT} \boldsymbol{D}_\mathrm{b} \tilde{\boldsymbol{B}}^k A^k + \tilde{\boldsymbol{B}}_\mathrm{s}^{kT} \boldsymbol{D}_\mathrm{s} \tilde{\boldsymbol{B}}_\mathrm{s}^k A^k \tag{53}$$

in which

$$\tilde{\boldsymbol{B}}^{kT} = \left[\tilde{\boldsymbol{B}}_{mj}^k \tilde{\boldsymbol{B}}_{bj}^k \right] \tag{54}$$

The advantage of the present ES-MITC3 as follows:

Using three-node triangular elements that are much easily generated automatically even for complicated geometry domains.

The ES-MITC3 element only uses the 3-node element with the same number of DOF as the MITC3 element, not increasing DOF to improve accuracy.

5. Accuracy of the proposed method

Firstly, we consider simple support (SSSS) and fully clamped (CCCC) FGP plates with three cases of distributions of porosity with parameter geometry $a = b = 1$ m, the thickness of the plate is constant $h = a/50$. Material properties are shown in Table 4 with power-law index $k = 1$ and maximum porosity value $\Omega = 0.5$. The maximum displacement of plate with different BC are presented in Table 1 and Fig. 6. The natural frequencies of the plate are shown in Table 2 and Fig. 7.

Secondly, the authors investigate a rectangular isotropic plate that has linear thickness variations in the x-directions and y-directions, length $a = 0.5$ m, $b = 2a$, $h_0 = 0.3$ m, $h_1 = h_2 = 0.2$ m, Young's moduli $E = 2$ GPa. The plate is one short-edge clamped, subjected to a uniform load $P = 2000$ Pa. Fig. 8 shows the

Table 1
Maximum displacements of the plate with different meshes.

Mesh	4 × 4	6 × 6	8 × 8	10 × 10	12 × 12	14 × 14	16 × 16	18 × 18	20 × 20
SSSS	0.5998	0.7935	0.8304	0.8434	0.8495	0.8529	0.8549	0.8563	0.8573
	0.6235	0.8343	0.8766	0.8913	0.8981	0.9019	0.9042	0.9057	0.9068
	0.7519	1.0291	1.0798	1.0968	1.1045	1.1087	1.1112	1.1129	1.1140
CCCC	0.1036	0.2581	0.3053	0.3174	0.3217	0.3234	0.3243	0.3247	0.3250
	0.1031	0.2862	0.3481	0.3645	0.3701	0.3725	0.3736	0.3742	0.3745
	0.1177	0.2950	0.3495	0.3635	0.3684	0.3704	0.3714	0.3719	0.3722

Please cite this article as: Tran TT et al., Static and free vibration analyses of functionally graded porous variable-thickness plates using an edge-based smoothed finite element method, Defence Technology, https://doi.org/10.1016/j.dt.2020.06.001

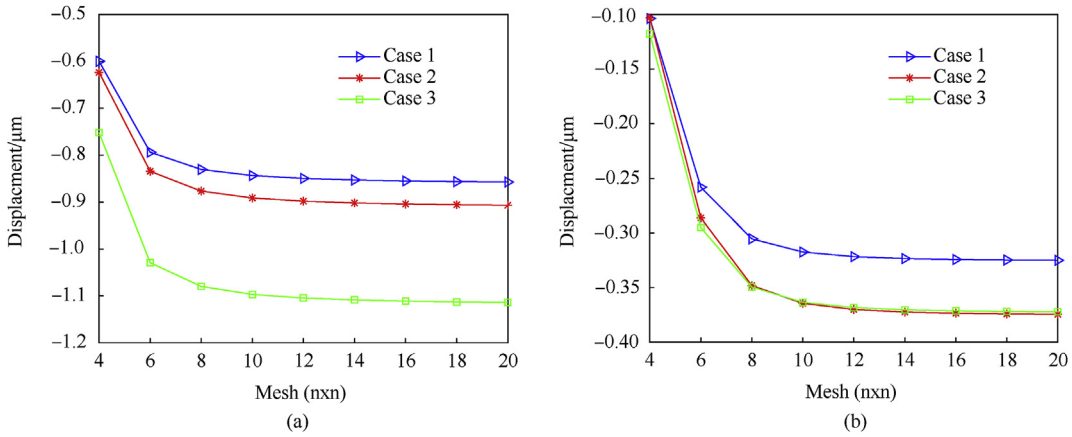

Fig. 6. The convergence of displacement of the plate with different meshes. a) The SSSS plate; b) The CCCC plate.

Table 2
Natural frequencies of the plate with different meshes.

Mesh	4 × 4	6 × 6	8 × 8	10 × 10	12 × 12	14 × 14	16 × 16	18 × 18	20 × 20
The first natural frequency λ_1									
SSSS	16.410	13.814	13.319	13.138	13.050	13.000	12.969	12.948	12.933
	15.399	12.882	12.391	12.211	12.125	12.076	12.045	12.025	12.011
	15.523	12.846	12.373	12.209	12.131	12.088	12.060	12.042	12.029
CCCC	43.374	25.416	22.678	21.946	21.659	21.517	21.436	21.385	21.351
	41.484	23.058	20.264	19.534	19.256	19.121	19.045	18.998	18.967
	43.252	25.268	22.527	21.796	21.509	21.368	21.287	21.236	21.202
The second natural frequency λ_2									
SSSS	41.485	33.878	31.689	30.824	30.400	30.159	30.008	29.907	29.836
	37.353	30.478	28.455	27.647	27.251	27.026	26.885	26.790	26.724
	40.741	33.243	31.101	30.264	29.858	29.629	29.486	29.391	29.325
CCCC	110.13	57.501	48.612	45.933	44.845	44.300	43.986	43.788	43.654
	105.17	52.299	43.560	40.954	39.913	39.401	39.111	38.929	38.806
	109.81	57.175	48.297	45.622	44.537	43.994	43.682	43.485	43.351

displacement at some points of the plate compared to the numerical results in Ref. [21]. It can be seen that the numerical results of present work are in good agreement with both value and shape in these comparisons.

Thirdly, let us consider the isotropic square plate with geometry parameters: $a = b = 1$ m; $h_0 = a/100$, the thickness varies linearly with the axis x: $h_x = h_0\left(1+\alpha\frac{x}{h}\right)$ with $\alpha = 0.1$ and material properties: $E = 2.1$ GPa $\upsilon = 0.3$, ρ =7850 kg/m^3 as shown in Ref. [22]. Non-dimensional natural frequencies $\omega^* = \sqrt[4]{\frac{\rho h_0 \omega^2 a^4}{D_0(1-\upsilon^2)}}$ with $D_0 = \frac{Eh_0^3}{12(1-\upsilon^2)}$ are shown in Table 3. The error results of the natural frequencies compared with those in Ref. [22] do not exceed 1%. From the results of comparison with reference solutions, it is shown that the proposed method ensures reliability and accuracy.

6. Numerical results and discussions

In this section, we use the material properties of the FGM plate from the study of Kim et al. [1]. The moduli and mass densities of two constituents are shown in Table 4.

6.1. Static bending of the FGP plates

In this subsection, we consider an SSSS FGP plate with dimension $a = b = 1$ m, $h_0 = a/50$, the thickness is varied linearly in x-axis and y-axis. The material properties of the FGP plate is shown in Table 2 with porosity distribution of case 1 in which $\Omega = 0.5$ and power-index $k = 1$. The plate subjected to uniform load with intensity $p = -1$ along z-axis. From Fig. 9(a) for plates with constant thickness $h_0 = h_1 = h_2 = a/50$, it can be seen that the deformation field is symmetric, and the maximum of deflection is at the center

Please cite this article as: Tran TT et al., Static and free vibration analyses of functionally graded porous variable-thickness plates using an edge-based smoothed finite element method, Defence Technology, https://doi.org/10.1016/j.dt.2020.06.001

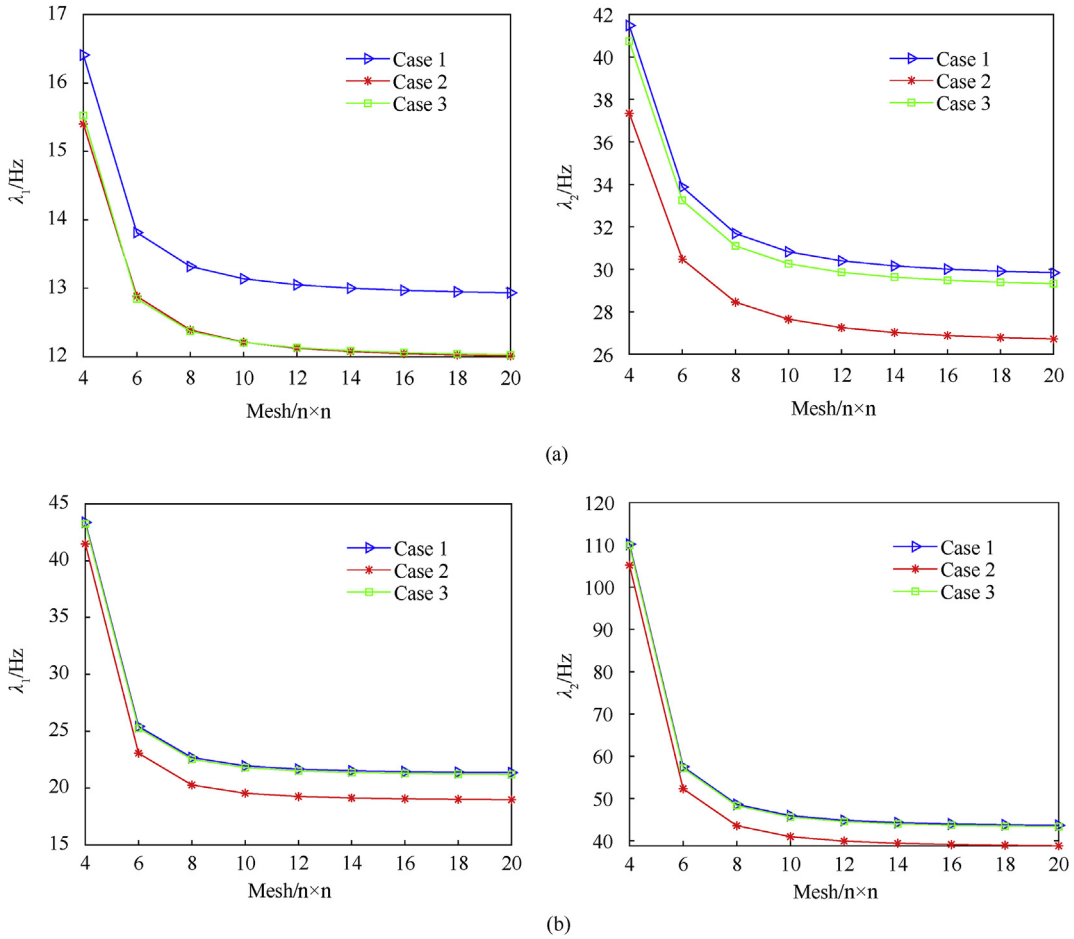

Fig. 7. The convergence of natural frequency of the plate with different meshes. a) The SSSS plate; b) the CCCC plate.

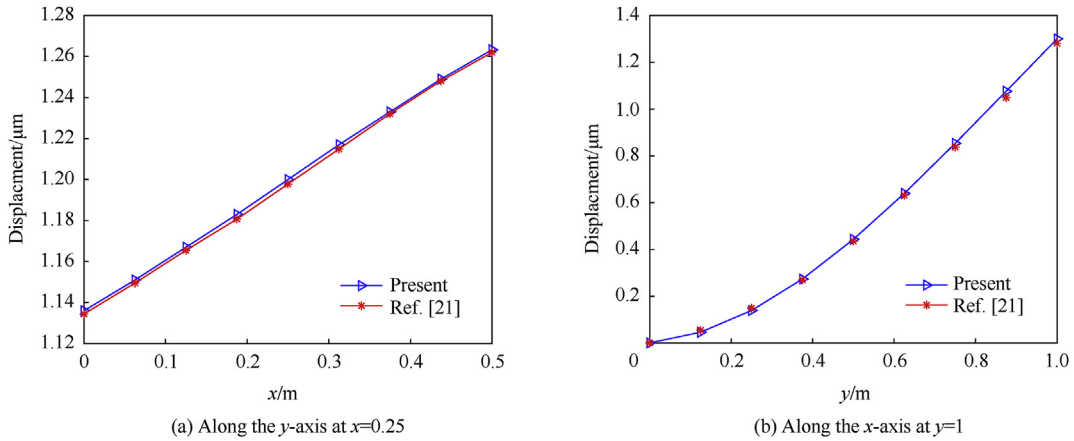

Fig. 8. Displacement at some points of the plate.

Table 3
Nondimensional natural frequencies ω^*.

ω^*	ω_1^*	ω_2^*	ω_3^*	ω_4^*	ω_5^*	ω_6^*
[22]	4.675	7.446	7.447	9.436	10.693	10.696
Present	4.675	7.419	7.437	9.446	10.589	10.594
$\% = 100\frac{\lvert\text{Present} - [22]\rvert}{[22]}$	0	0.36	0.13	0.11	0.97	0.95

Please cite this article as: Tran TT et al., Static and free vibration analyses of functionally graded porous variable-thickness plates using an edge-based smoothed finite element method, Defence Technology, https://doi.org/10.1016/j.dt.2020.06.001

Table 4
Material properties of the FGP plate.

Material properties	Young's moduli/GPa	Mass densities/(kg/m^{-3})	Poisson's ratio
Top surface (ceramic)	$E_t = 14.4$	$\rho_t = 12200$	$\upsilon = 0.38$
Bottom surface (metal)	$E_b = 1.44$	$\rho_b = 1220$	$\upsilon = 0.38$

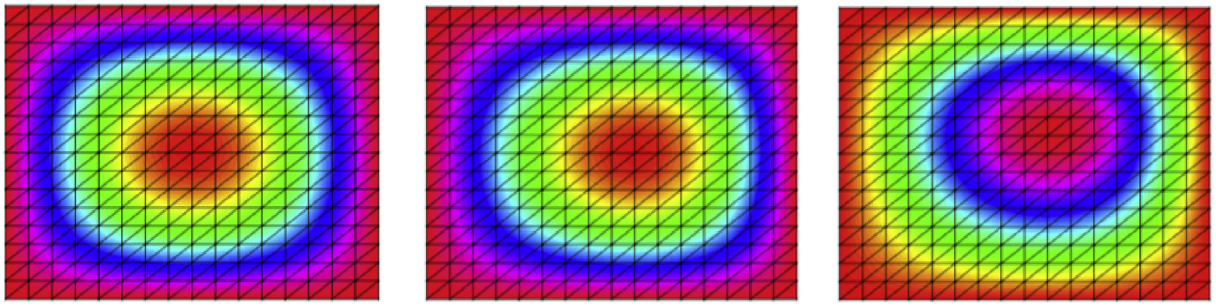

(a) Plate has a constant thickness (type 1)

(b) Thickness varies linearly in x-axis (type 2)

(c) Thickness varies linearly in x-axis and y-axis(type 3)

Fig. 9. The visualization of the deformation of an SSSS FGP plate (top view).

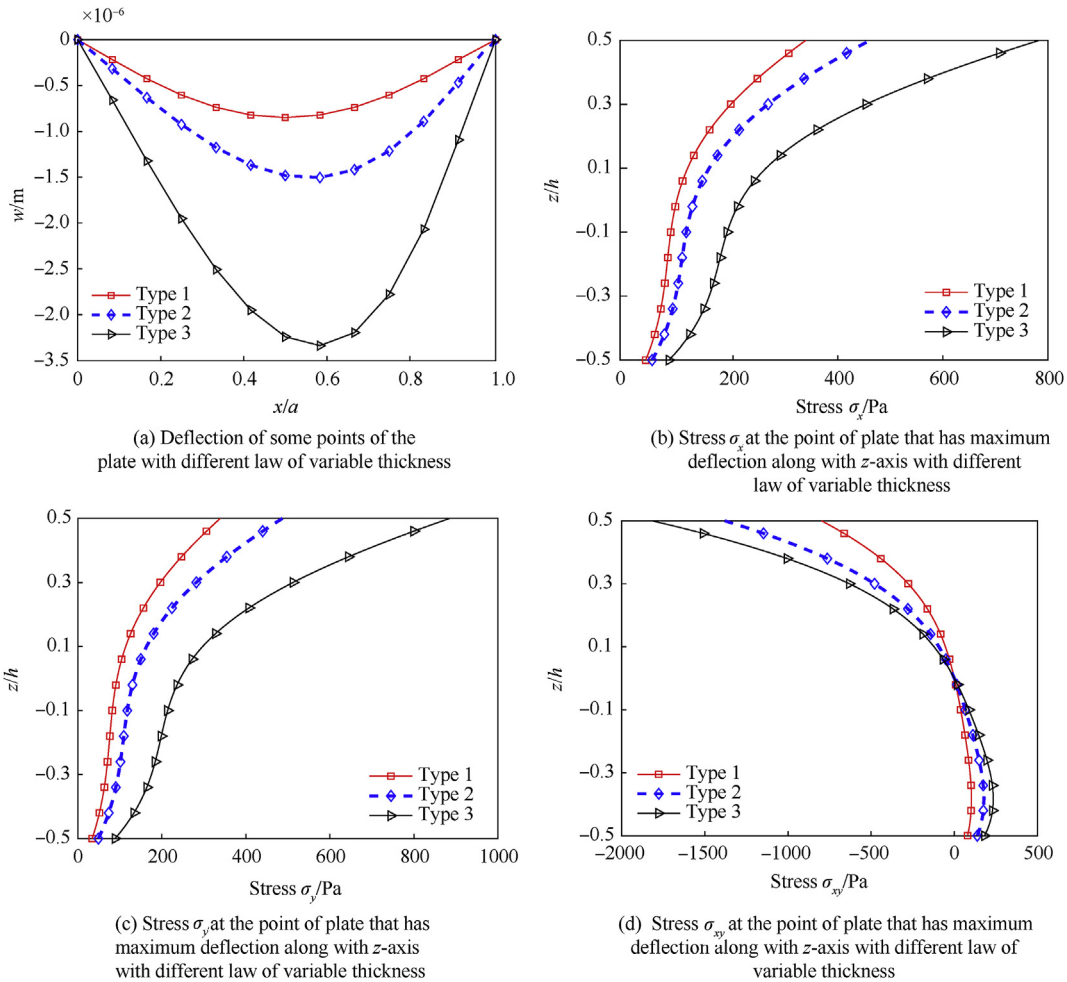

(a) Deflection of some points of the plate with different law of variable thickness

(b) Stress σ_x at the point of plate that has maximum deflection along with z-axis with different law of variable thickness

(c) Stress σ_y at the point of plate that has maximum deflection along with z-axis with different law of variable thickness

(d) Stress σ_{xy} at the point of plate that has maximum deflection along with z-axis with different law of variable thickness

Fig. 10. Displacement at some points of the plate and stress at the point of plate that has maximum deflection along with z-axis.

of the plate. However, the deflection of the plate with variable thickness is not symmetric, the maximum of deflection will be near the thinner thickness and far away from thicker thickness as shown in Fig. 9(b and c).

Please cite this article as: Tran TT et al., Static and free vibration analyses of functionally graded porous variable-thickness plates using an edge-based smoothed finite element method, Defence Technology, https://doi.org/10.1016/j.dt.2020.06.001

Table 5
Maximum of deflection of the FGP plate.

Law of variable thickness	Type 1	Type 2	Type 3
Maximum displacement w/μm	0.84940	1.50410	3.44820
Maximum stress σ_x/Pa	338.8142	461.0199	783.4902
Maximum stress σ_y/Pa	338.8142	486.9305	885.1117
Maximum stress σ_{xy}/Pa	102.9081	177.9914	234.3172

Table 6
The maximum deflection of FGP plate (type 3) with different values of k (μm).

Ω	k	0	2	4	6	8	10
0.25	Case 1	1.487	3.980	4.815	5.246	5.578	5.867
	Case 2	1.594	4.074	5.008	5.492	5.853	6.165
	Case 3	1.594	4.435	5.377	5.880	6.276	6.623
0.5	Case 1	1.640	4.450	5.310	5.744	6.078	6.371
	Case 2	1.951	4.759	5.916	6.504	6.921	7.273
	Case 3	1.951	5.827	6.997	7.632	8.145	8.596
0.75	Case 1	1.828	5.096	5.962	6.385	6.717	7.010
	Case 2	2.608	5.988	7.644	8.490	9.041	9.473
	Case 3	2.608	8.883	10.563	11.489	12.252	12.918
1	Case 1	2.066	6.125	6.902	7.277	7.595	7.884
	Case 2	5.037	9.528	13.471	16.064	17.654	18.687
	Case 3	5.037	26.914	33.995	38.384	41.691	44.063

In Fig. 10(a), the deflection of some points along x-aix with y =0.5 m (type 1, type 2) and y =7/12 (type 3) are presented. Fig. 10(b–d) show the stress at the point of plate that has maximum deflection. Maximum of deflection and stress are shown in Table 5. This phenomenon shows that the variation of plate thickness significant effects on the static bending response of the FGP plate.

In order to investigate the effect of power-index k to static bending of the FGP plate. We change the k from 0 to 10 for all cases of porosity distribution. From Fig. 11 and Table 6, it can be observed that with the same Ω value, the maximum deflection of FGP plate in porosity distribution of case 3 is greatest and the smallest result is for the porosity distribution of case 1. When k increases, the volume of metal increases, the stiffness of the FGP plate will be reduced and hence the deflection increases.

Next, the authors investigate the effect of maximum porosity value Ω on bending of the FGP plate. Maximum porosity values are chosen as Ω = 0, 0.2, 0.4, 0.6, 0.8, 1 for all cases of porosity distribution. From to Fig. 12 and Table 7, when k = 0 (the material of the plate is ceramic), it can be seen that the deflection of FGP plate in porosity distribution of case 1 is the smallest, and the deflection of FGP plate with porosity distribution of case 2 and case 3 are the same. These results are appropriate because, with the homogeneous FGP plate, the porosity distributions of cases 2 and 3 are symmetric, and the values of stiffness obtained are not different. With k not equal to zero, the deflection of FGP plate in porosity

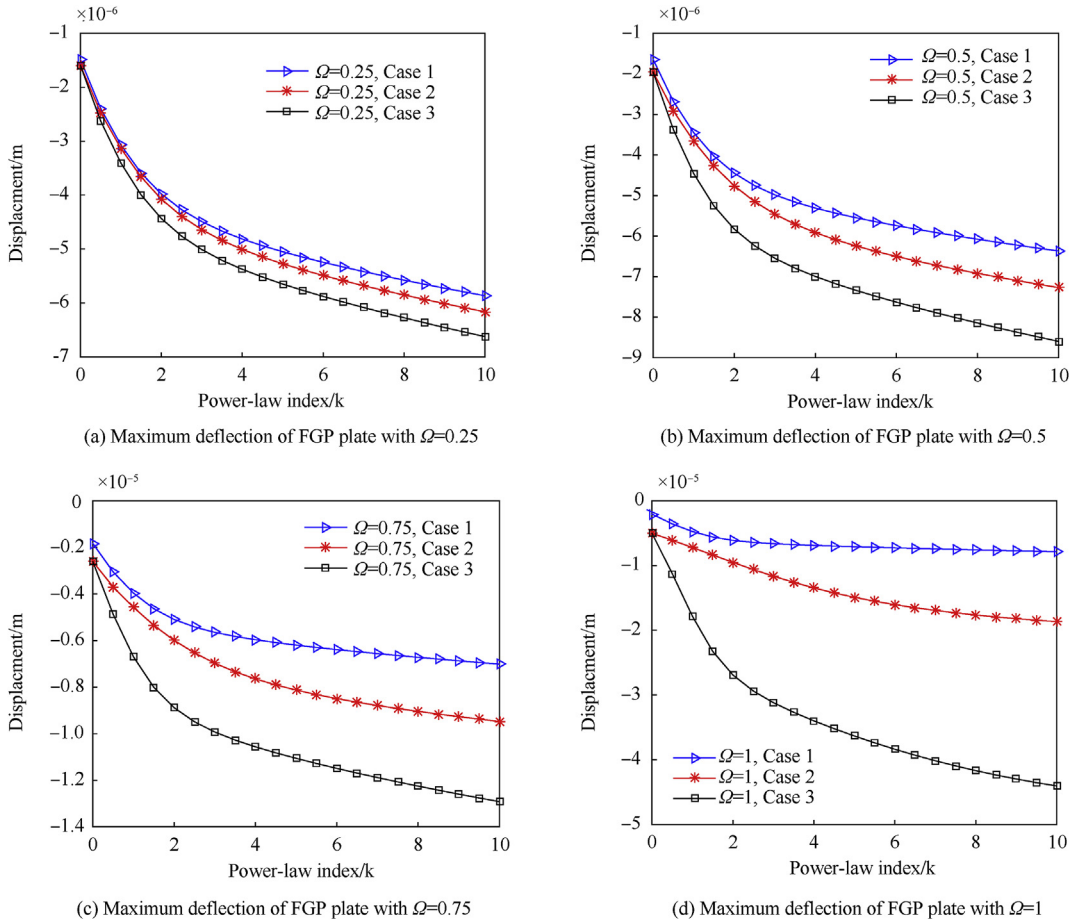

(a) Maximum deflection of FGP plate with Ω=0.25

(b) Maximum deflection of FGP plate with Ω=0.5

(c) Maximum deflection of FGP plate with Ω=0.75

(d) Maximum deflection of FGP plate with Ω=1

Fig. 11. The maximum deflection of FGP plate (type 3) with different of values of k.

Please cite this article as: Tran TT et al., Static and free vibration analyses of functionally graded porous variable-thickness plates using an edge-based smoothed finite element method, Defence Technology, https://doi.org/10.1016/j.dt.2020.06.001

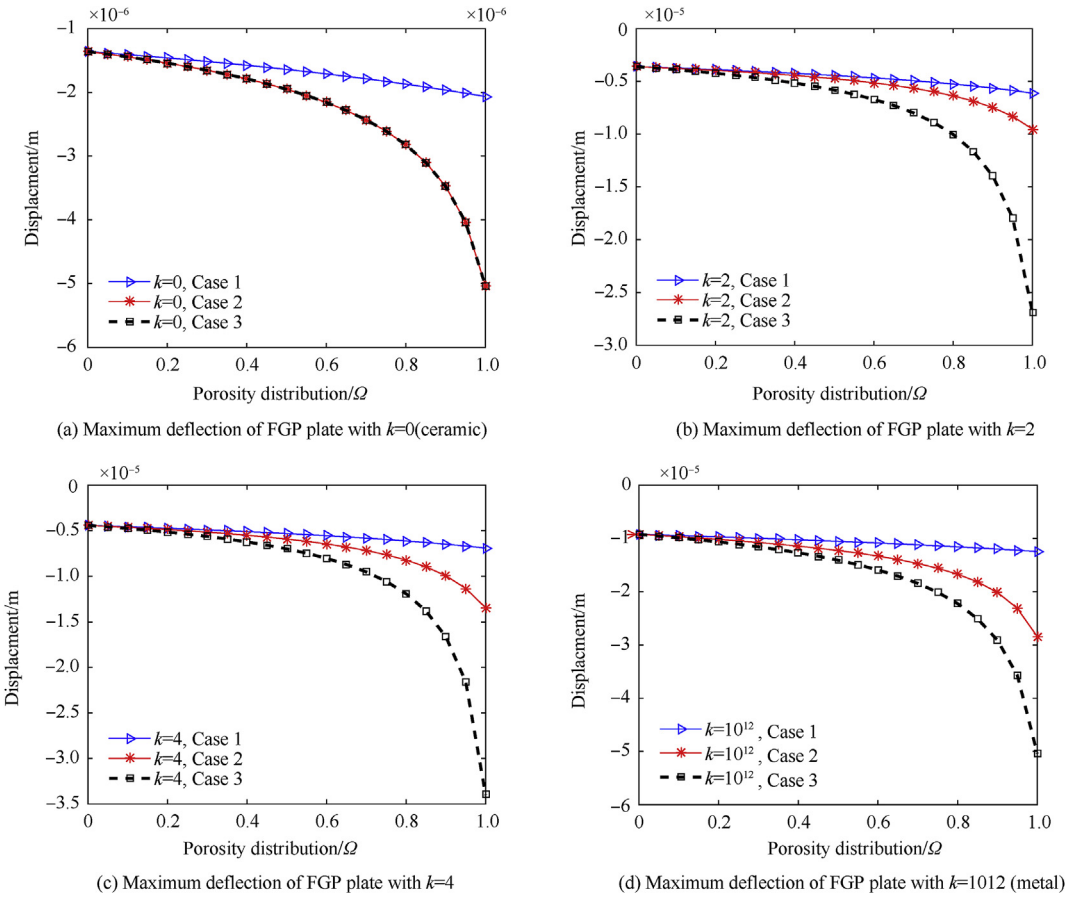

Fig. 12. The maximum deflection of FGP plate (type 3) with different values of k.

Table 7
The maximum deflection of FGP plate (type 3) with different values of Ω (μm).

k	Ω	0	0.2	0.4	0.6	0.8	1
0	Case 1	1.359	1.459	1.575	1.710	1.871	2.066
	Case 2	1.359	1.540	1.787	2.157	2.824	5.036
	Case 3	1.359	1.540	1.787	2.157	2.824	5.036
2	Case 1	3.613	3.899	4.246	4.680	5.259	6.124
	Case 2	3.613	3.969	4.446	5.150	6.379	9.527
	Case 3	3.613	4.239	5.166	6.717	10.037	26.914
4	Case 1	4.418	4.729	5.098	5.547	6.120	6.902
	Case 2	4.418	4.872	5.497	6.452	8.224	13.471
	Case 3	4.418	5.148	6.228	8.033	11.922	33.995
10^{12}	Case 1	9.222	9.699	10.236	10.851	11.571	12.448
	Case 2	9.222	10.166	11.432	13.306	16.710	28.393
	Case 3	9.222	10.646	12.681	15.911	22.234	50.367

Table 8
Natural frequencies of the FGP plate.

f_1/Hz	f_2/Hz	f_3/Hz	f_4/Hz	f_5/Hz	f_6/Hz
8.1743	18.7768	19.2096	31.6758	38.4102	39.0436

distribution of case 1 is the smallest, and the largest is for the porosity distribution of case 3. This also proves that when the porosity is more distributed on the upper surface of the FGP plate according to thickness, stiffness of the plate is reduced (case 3).

6.2. Free vibration of FGP plates

In this subsection, an SSSS FGP plate is considered with geometric parameters: $a = b = 1$ m, $h_0 = a/50$, the thickness is varied linearly in x-axis and y-axis (type 3). The material properties of the FGP plate are similar to the static bending problem with porosity distribution $\Omega = 0.5$ and power-index $k = 1$. The first six natural frequencies of the FGP plate are shown in Table 8 and the first six mode shape are presented in Fig. 13. In these figures, the mode shape of vibration of the variable-thickness FGP plate is not symmetric because the thickness at each position on the plate is different. The maximum values of the mode shape are traveled toward a smaller thickness.

Now, we investigate the influence of power-law index k on free vibration of the FGP plate. Power-law index gets values $k = 0, 2, 4, 6, 8, 10$ for all cases of porosity distribution. In Fig. 14 and Table 9, it can be seen that with the same Ω value, the first natural frequency

Please cite this article as: Tran TT et al., Static and free vibration analyses of functionally graded porous variable-thickness plates using an edge-based smoothed finite element method, Defence Technology, https://doi.org/10.1016/j.dt.2020.06.001

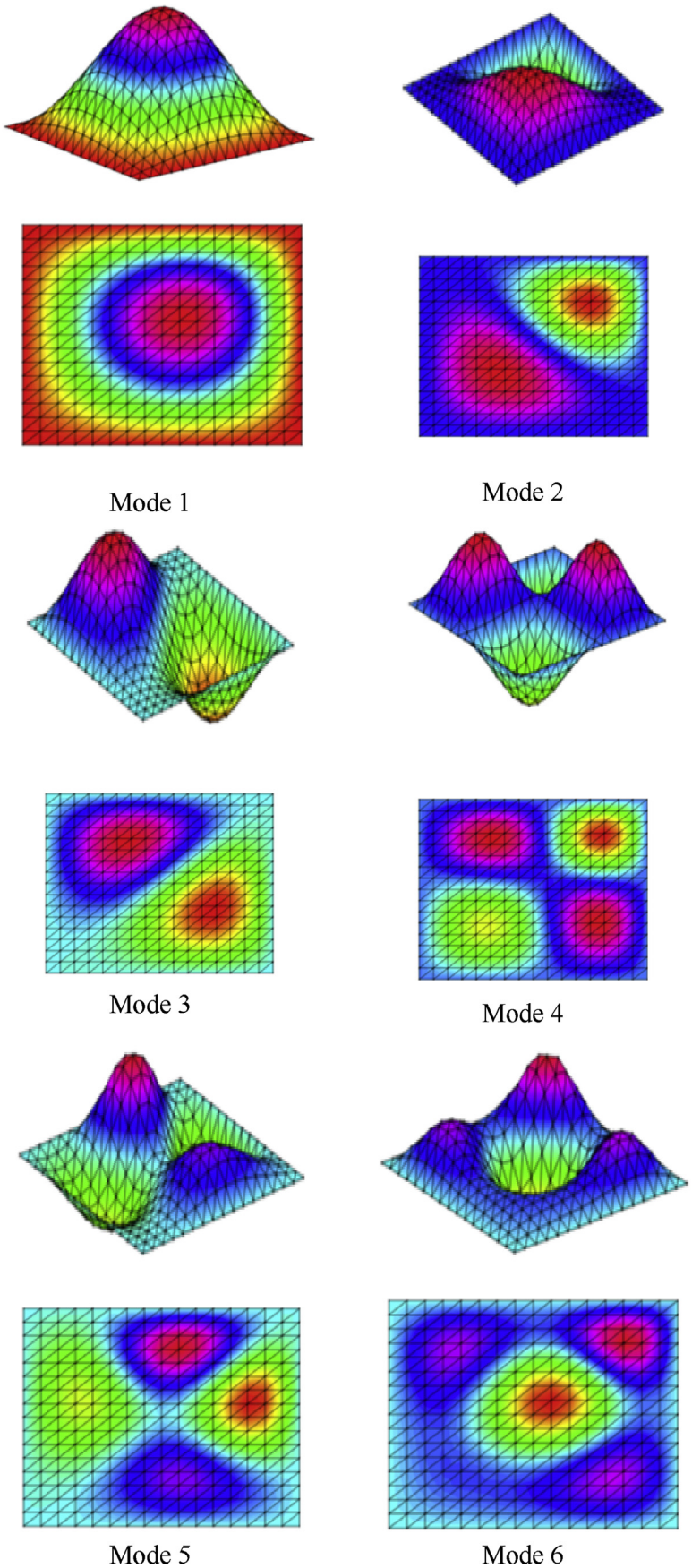

Fig. 13. The first six mode shapes of the FGP plate (type 3).

Please cite this article as: Tran TT et al., Static and free vibration analyses of functionally graded porous variable-thickness plates using an edge-based smoothed finite element method, Defence Technology, https://doi.org/10.1016/j.dt.2020.06.001

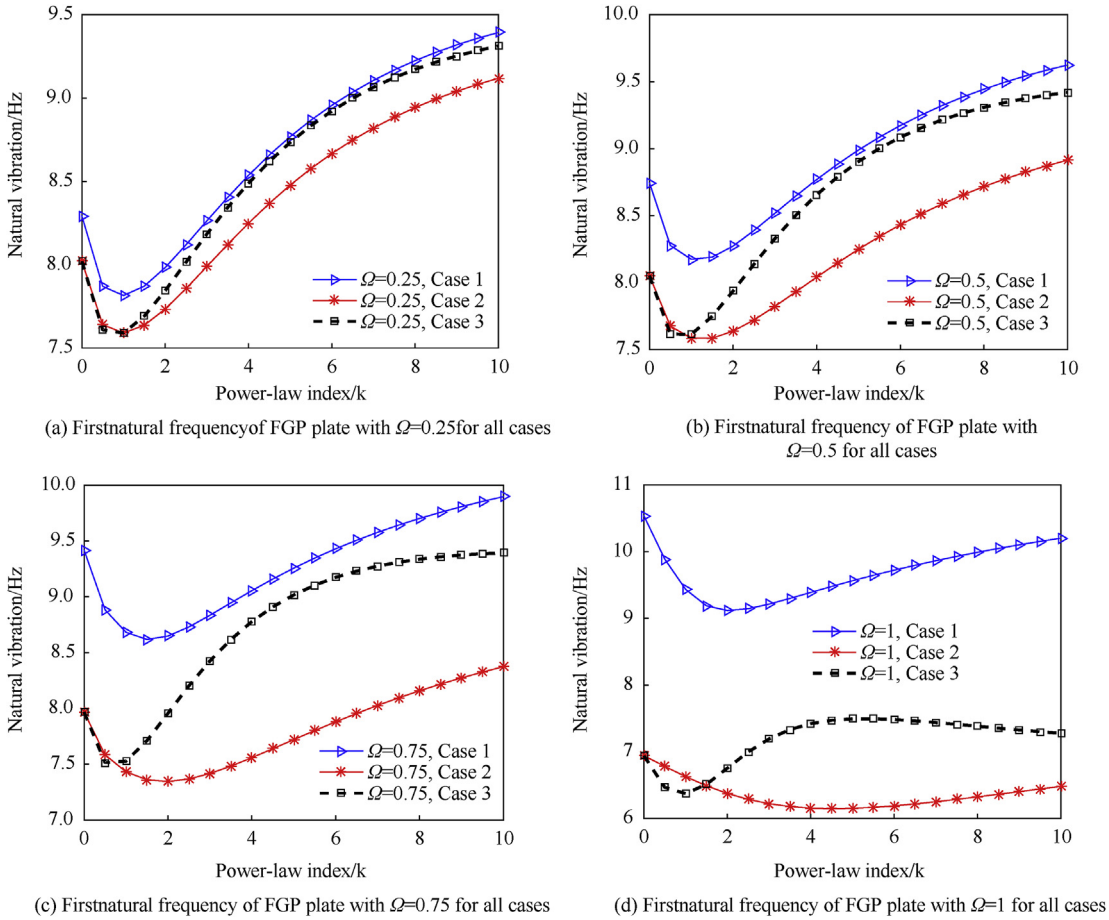

(a) Firstnatural frequencyof FGP plate with Ω=0.25for all cases

(b) Firstnatural frequency of FGP plate with Ω=0.5 for all cases

(c) Firstnatural frequency of FGP plate with Ω=0.75 for all cases

(d) Firstnatural frequency of FGP plate with Ω=1 for all cases

Fig. 14. The first natural frequencies of FGP plate with different values of *k*.

Table 9
The first natural frequencies of the FGP plate with different values of *k* (Hz).

Ω	*k*	0	2	4	6	8	10
0.25	Case 1	8.292	7.983	8.536	8.956	9.224	9.392
	Case 2	8.021	7.735	8.249	8.667	8.943	9.118
	Case 3	8.021	7.845	8.489	8.922	9.172	9.312
0.5	Case 1	8.745	8.273	8.770	9.173	9.444	9.625
	Case 2	8.053	7.638	8.041	8.432	8.718	8.915
	Case 3	8.053	7.938	8.657	9.085	9.309	9.421
0.75	Case 1	9.418	8.648	9.054	9.430	9.701	9.897
	Case 2	7.967	7.345	7.558	7.880	8.158	8.374
	Case 3	7.967	7.956	8.777	9.173	9.337	9.393
1	Case 1	10.537	9.118	9.390	9.723	9.991	10.204
	Case 2	6.941	6.376	6.155	6.189	6.324	6.482
	Case 3	6.941	6.755	7.422	7.484	7.383	7.276

of the FGP plate in porosity distribution of case 1 is greatest, and the smallest is for the porosity distribution of case 3. With $\Omega = 0.25, 0.5, 0.75$ when *k* increases from 0 to 1, the first natural frequencies of the FGP plate will be reduced, but *k* increases from 1 to 10 when the first natural frequencies of the FGP plate will increase. However, with $\Omega = 1$ the first natural frequencies of the FGP plate with porosity distribution of case 1 and case 2 increase when *k* changes from 2 to 10. In case 3 the first natural frequencies of the FGP plate increase from 4 to 10.

Finally, the effect of maximum porosity distribution on the free vibration of the FGP plate (type 3) is considered. The value of maximum porosity Ω changes from 0 to 1 for all cases of porosity distribution. From Fig. 15 to Table 10, in can be found that when $k = 0$ (the material of plate is ceramic), the first natural frequencies of FGP plate in porosity distribution of case 1 increase, the first natural frequencies in case 2 and case 3 are similar. With *k* varies from zero, the first natural frequency of FGP plate in porosity distribution of case 1 is the largest, and the smallest is for the porosity distribution of case 3.

7. Conclusions

In this paper, the static and free vibration analyses of the FGP variable-thickness plates are studied using the ES-MITC3. Numerical results of static bending and free vibration obtained by the present approach are compared to other available solutions. From the present formulation and the numerical results, we can withdraw some following points:

- For static and free vibration analyses of the FGP variable-thickness plates, the ES-MITC3 element which can eliminate "the shear locking" phenomenon will give the more accurate results than the standard triangular elements and the original MITC3 element.
- The law of variable thickness significant effects on displacement, stress, and free vibration of the plates. The material parameters also change the stiffness and mass of the plates. Specifically, with the same geometry and BC, when the power-index *k* increases, the "stiffness" of the plate will decrease and when the maximum porosity distributions Ω increase, the "stiffness" of plate will decrease, respectively.

Please cite this article as: Tran TT et al., Static and free vibration analyses of functionally graded porous variable-thickness plates using an edge-based smoothed finite element method, Defence Technology, https://doi.org/10.1016/j.dt.2020.06.001

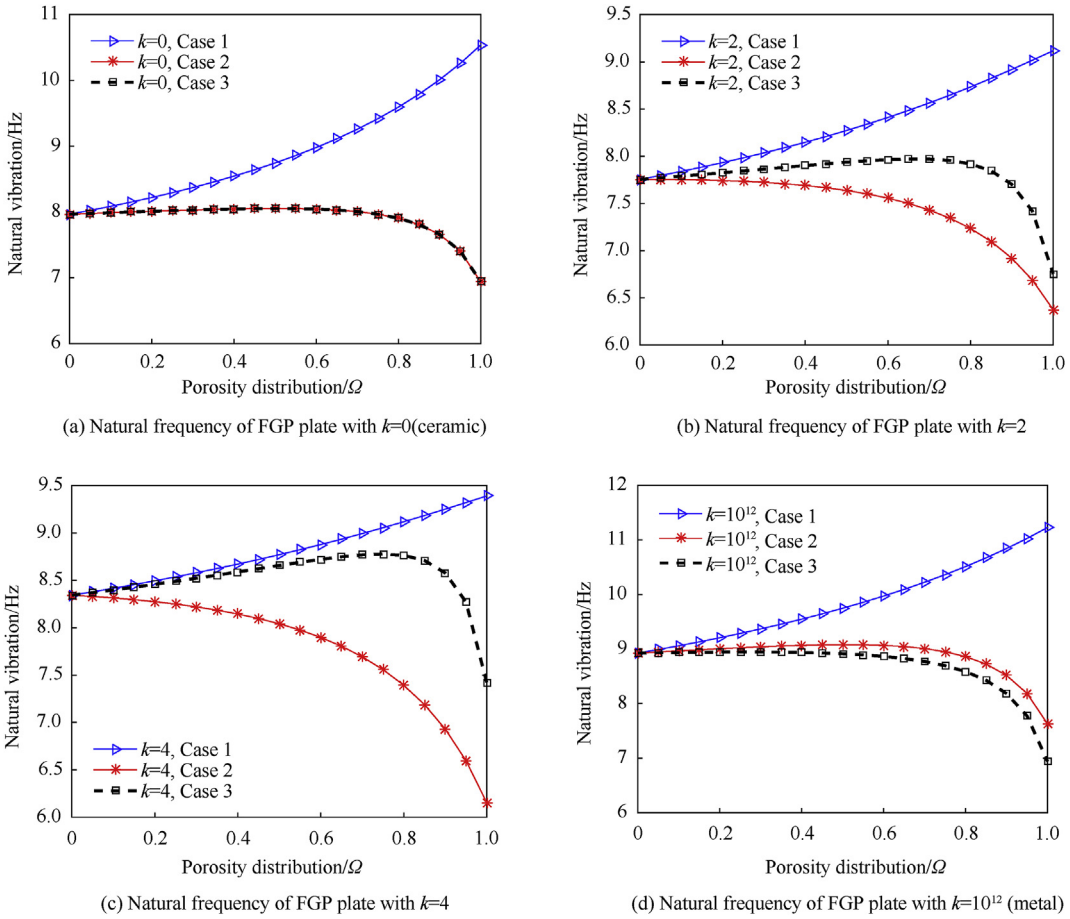

(a) Natural frequency of FGP plate with k=0(ceramic)

(b) Natural frequency of FGP plate with k=2

(c) Natural frequency of FGP plate with k=4

(d) Natural frequency of FGP plate with k=10^{12} (metal)

Fig. 15. Natural frequencies of the FGP plate with different values of Ω.

Table 10
The natural frequencies of the FGP plate with different values of Ω (Hz).

k	Ω	0	0.2	0.4	0.6	0.8	1
0	Case 1	7.966	8.219	8.544	8.979	9.594	10.537
	Case 2	7.966	8.011	8.046	8.044	7.906	6.941
	Case 3	7.966	8.011	8.046	8.044	7.906	6.941
2	Case 1	7.755	7.933	8.149	8.412	8.735	9.118
	Case 2	7.755	7.743	7.691	7.557	7.236	6.376
	Case 3	7.755	7.826	7.902	7.965	7.919	6.755
4	Case 1	8.343	8.495	8.671	8.877	9.118	9.390
	Case 2	8.343	8.274	8.145	7.898	7.393	6.155
	Case 3	8.343	8.458	8.588	8.721	8.763	7.422
10^{12}	Case 1	8.925	9.206	9.547	9.970	10.510	11.225
	Case 2	8.925	9.005	9.067	9.067	8.860	7.629
	Case 3	8.925	8.942	8.936	8.865	8.586	6.941

- Numerical results in present work are useful for calculation, design, and testing of material parameters in engineering and technologies.
- The present approach can be developed for investigating the plates with laws of variable thickness and also for analysing the FGP plates subjected to other loads.

Data availability

The data used to support the findings of this study are included within the article.

Declaration of competing interest

The authors declare that they have no conflicts of interest.

Acknowledgments

This research is funded by Vietnam National Foundation for Science and Technology Development (NAFOSTED) under Grant number 107.02–2019.330.

References

[1] Kim Jinseok, Żur Krzysztof Kamil, Reddy JN. Bending, free vibration, and buckling of modified couples stress-based functionally graded porous micro-plates. Compos Struct 2019;209:879–88.
[2] Barati Mohammad Reza, Zenkour Ashraf M. Vibration analysis of functionally graded graphene platelet reinforced cylindrical shells with different porosity distributions. Mech Adv Mater Struct 2019;26(6):503–11.
[3] Zenkour AM. Quasi-3D refined theory for functionally graded porous plates: displacements and stresses. Phys Mesomech 2020;23:39–53.
[4] Barati Mohammad Reza, Zenkour Ashraf M. Electro-thermoelastic vibration of plates made of porous functionally graded piezoelectric materials under various boundary conditions. J Vib Contr 2018;24(10):1910–26.
[5] Barati Mohammad Reza, Zenkour Ashraf M. Analysis of postbuckling of graded porous GPL-reinforced beams with geometrical imperfection. Mech Adv Mater Struct 2019;26(18):1580–8.
[6] Ahmed Amine Daikh, Zenkour Ashraf M. Effect of porosity on the bending analysis of various functionally graded sandwich plates. Mater Res Express 2019;6(6):065703.
[7] Zenkour Ashraf, Ahmed Amine Daikh. Free vibration and buckling of porous power-law and sigmoid functionally graded sandwich plates using a simple higher-order shear deformation theory. Mater Res Express 2019;6(11):115707.
[8] Sobhy Mohammed, Ashraf M Zenkour. Porosity and inhomogeneity effects on

the buckling and vibration of doubleFGM nanoplates via a quasi-3D refned theory. Compos Struct 2019;220:289–303.
[9] Mashat Daoud S, Zenkour Ashraf M, Radwan Ahmed F. A quasi 3-D higher-order plate theory for bending of FG plates resting on elastic foundations under hygro-thermo-mechanical loads with porosity. Eur J Mech Solid 2020;82:103985.
[10] Nguyen Nam V, Nguyen Hoang X, Lee Seunghye, Nguyen-Xuan H. Geometrically nonlinear polygonal finite element analysis of functionally graded porous plates. Adv Eng Software 2018;126:110–26.
[11] Nguyen Nam V, Nguyen-Xuan H, Lee Dongkyu, Lee Jaehong. A novel computational approach to functionally graded porous plates with graphene platelets reinforcement. Thin-Walled Struct 2020;150:106684.
[12] Nguyen Nam V, Lee Jaehong, Nguyen-Xuan H. Active vibration control of GPLs-reinforced FG metal foam plates with piezoelectric sensor and actuator layers. Composites Part B 2019;172:769–84.
[13] Nguyen Nam V, Nguyen Lieu B, Nguyen-Xuan H, Lee Jaehong. Analysis and active control of geometrically nonlinear responses of smart FG porous plates with graphene nanoplatelets reinforcement based on Bézier extraction of NURBS. Int J Mech Sci 2020:105692.
[14] Rezaei AS, Saidi AR. Application of Carrera Unified Formulation to study the effect of porosity on natural frequencies of thick porous–cellular plates. Compos B Eng 2016;91:361–70.
[15] Rezaei AS, Saidi AR. Exact solution for free vibration of thick rectangular plates made of porous materials. Compos Struct 2015;134:1051–60.
[16] Zhao J, Xie F, Wang A, Shuai C, Tang J, Wang Q. A unified solution for the vibration analysis of functionally graded porous (FGP) shallow shells with general boundary conditions. Compos B Eng 2019;156:406–24.
[17] Zhao J, Xie F, Wang A, Shuai C, Tang J, Wang Q. Vibration behavior of the functionally graded porous (FGP) doubly-curved panels and shells of revolution by using a semi-analytical method. Compos B Eng 2019;157:219–38.
[18] Li Q, Wu D, Chen X, Liu L, Yu Y, Gao W. Nonlinear vibration and dynamic buckling analyses of sandwich functionally graded porous plate with graphene platelet reinforcement resting on Winkler–Pasternak elastic foundation. Int J Mech Sci 2018;148:596–610.
[19] Sahmani S, Aghdam MM, Rabczuk T. Nonlocal strain gradient plate model for nonlinear large-amplitude vibrations of functionally graded porous micro/nano-plates reinforced with GPLs. Compos Struct 2018;198:51–62.
[20] Wu D, Liu A, Huang Y, Huang Y, Pi Y, Gao W. Dynamic analysis of functionally graded porous structures through finite element analysis. Eng Struct 2018;165:287–301.
[21] Gagnon P, Gosseln C. The finite strip element for the analysis of variable thickness rectangular plate. Comput Struct 1997;63(2):349–62.
[22] Sakiyama M Huang. Free vibration analysis of rectangular plate with variable thickness. J Sound Vib 1998;216(3):379–97.
[23] Singh B, Saxena V. Transverse vibration of a rectangular plate with bidirectional thickness variation. J Sound Vib 1996;198:51–6.
[24] Nerantzaki MS, Katsikadelis JT. An analog equation solution to dynamic analysis of plates with variable thickness. Eng Anal Bound Elem 1996;17:145–52.
[25] Mikami T, Yoshimura J. Application of the collocation method to vibration analysis of rectangular Mindlin plates. Comput Struct 1984;18:425–31.
[26] Aksu G, Al-Kaabi SA. Free vibration analysis of mindlin plates with linearly varying thickness. J Sound Vib 1987;119:189–205.
[27] Al-Kaabi SA, Aksu G. Free vibration analysis of mindlin plates with parabolically varying thickness. Comput Struct 1989;33:1417–21.
[28] Mizusawa T. Vibration of rectangular mindlin plates with tapered thickness by the spline strip method. Comput Struct 1993;44:451–63.
[29] Cheung YK, Zhou D. Vibration of tapered mindlin plates in terms of static timoshenko beam functions. J Sound Vib 2003;260:693–709.
[30] Le-Manh T, Huynh-Van Q, Phan Thu D, Phan Huan D, Nguyen-Xuan H. Isogeometric nonlinear bending and buckling analysis of variable-thickness composite plate structures. Compos Struct 2017;159:818–26.
[31] Lieu QX, Lee S, Kang J, Lee J. Bending and free vibration analyses of in-plane bi directional functionally graded plates with variable thickness using isogeometric analysis. Compos Struct 2018;192:434–51.
[32] Gupta A, Jain NK, Salhotra R, Joshi PV. Effect of crack location on vibration analysis of partially cracked isotropic and FGM micro-plate with non-uniform thickness: an analytical approach. Int J Mech Sci 2018;145:410–29.
[33] Dhurvey P. Buckling analysis of composite laminated skew plate of variable thickness. Mater Today: Proceedings 2017;4(9):9732–6.
[34] Thang Pham-Toan, Nguyen-Thoi T, Lee Jaehong. Closed-form expression for nonlinear analysis of imperfect sigmoid-FGM plates with variable thickness resting on elastic medium. Compos Struct 2016;143:143–50.
[35] Banh-Thien T, Dang-Trung H, Le-Anh L, Ho-Huu V, Nguyen-Thoi T. Buckling analysis of non-uniform thickness nanoplates in an elastic medium using the Isogeometric analysis. Compos Struct 2017;162:182–93.
[36] Zenkour Ashraf M. Bending of thin rectangular plates with variable-thickness in a hygrothermal Environment. Thin-Walled Struct 2018;123:333–40.
[37] Allam Mohammed NM, Tantawy Rania, Zenkour Ashraf M. Thermoelastic stresses in functionally graded rotating annular disks with variable thickness. J Theor Appl Mech 2018;56(4):1029–41.
[38] Lee P-S, Bathe K-J. Development of MITC isotropic triangular shell finite elements. Comput Struct 2004;82:945–62.
[39] Liu G, Nguyen-Thoi T, Lam K. An edge-based smoothed finite element method (ES-FEM) for static, free and forced vibration analyses of solids. J Sound Vib 2009;320:1100–30.
[40] Chau-Dinh T, Nguyen-Duy Q, Nguyen-Xuan H. Improvement on MITC3 plate finite element using edge-based strain smoothing enhancement for plate analysis. Acta Mech 2017;228:2141–63.
[41] Nguyen T-K, Nguyen V-H, Chau-Dinh T, Vo TP, Nguyen-Xuan H. Static and vibration analysis of isotropic and functionally graded sandwich plates using an edge-based MITC3 finite elements. Compos B Eng 2016;107:162–73. 2016/12/15.
[42] Pham Q-H, Tran T-V, Pham T-D, Phan D-H. An edge-based smoothed MITC3 (ES-MITC3) shell finite element in laminated composite shell structures analysis. Int J Comput Methods 2017:1850060.
[43] Pham Quoc-Hoa, Pham Tien-Dat, Quoc V Trinh, Phan Duc-Huynh. Geometrically nonlinear analysis of functionally graded shells using an edge-based smoothed MITC3 (ES-MITC3) finite elements. Eng Comput 2019:1–14.
[44] Pham-Tien D, Pham-Quoc H, Vu-Khac T, Nguyen-Van N. Transient analysis of laminated composite shells using an edge-based smoothed finite element method. In: International conference on advances in computational mechanics; 2017. p. 1075–94.
[45] Tran Trung Thanh, Pham Quoc-Hoa, Nguyen-Thoi Trung. An edge-based smoothed finite element for free vibration analysis of functionally graded porous (FGP) plates on elastic foundation taking into mass (EFTIM). Math Probl Eng 2020. https://doi.org/10.1155/2020/8278743.
[46] Bletzinger Kai-Uwe, Bischoff Manfred, Ramm Ekkehard. A unified approach for shear-locking-free triangular and rectangular shell finite elements. Comput Struct 2000;75(3):321–34.
[47] Nguyen-Thoi T, Phung-Van P, Nguyen-Xuan H, Thai Chien H. A cell-based smoothed discrete shear gap method (CS-DSG3) using triangular elements for static and free vibration analyses of Reissner-Mindlin plates. Int J Numer Methods Eng 2012;91(7):705–41.
[48] Bathe Klaus-Jürgen, Dvorkin Eduardo N. A formulation of general shell elements-the use of mixed interpolation of tensorial components. Int J Numer Methods Eng 1986;22(3):697–722.
[49] Reddy JN. Mechanics of laminated composite plates and shells: theory and analysis. second ed. Boca Raton Florida: CRC Press; 2004.

Please cite this article as: Tran TT et al., Static and free vibration analyses of functionally graded porous variable-thickness plates using an edge-based smoothed finite element method, Defence Technology, https://doi.org/10.1016/j.dt.2020.06.001